3-D photoacoustic and pulse echo imaging of prostate tumor progression in the mouse window chamber

Daniel R. Bauer, Ragnar Olafsson, Leonardo G. Montilla, and Russell S. Witte
University of Arizona, Department of Radiology, 1609 North Warren Avenue, Tucson, Arizona 85724

Abstract. Understanding the tumor microenvironment is critical to characterizing how cancers operate and predicting their response to treatment. We describe a novel, high-resolution coregistered photoacoustic (PA) and pulse echo (PE) ultrasound system used to image the tumor microenvironment. Compared to traditional optical systems, the platform provides complementary contrast and important depth information. Three mice are implanted with a dorsal skin flap window chamber and injected with PC-3 prostate tumor cells transfected with green fluorescent protein. The ensuing tumor invasion is mapped during three weeks or more using simultaneous PA and PE imaging at 25 MHz, combined with optical and fluorescent techniques. Pulse echo imaging provides details of tumor structure and the surrounding environment with 100-μm^3 resolution. Tumor size increases dramatically with an average volumetric growth rate of 5.35 mm^3/day, correlating well with 2-D fluorescent imaging ($R = 0.97$, $p < 0.01$). Photoacoustic imaging is able to track the underlying vascular network and identify hemorrhaging, while PA spectroscopy helps classify blood vessels according to their optical absorption spectrum, suggesting variation in blood oxygen saturation. Photoacoustic and PE imaging are safe, translational modalities that provide enhanced depth resolution and complementary contrast to track the tumor microenvironment, evaluate new cancer therapies, and develop molecular contrast agents *in vivo*.
[DOI: 10.1117/1.3540668]

Keywords: optoacoustics; ultrasound; dorsal skin flaps; prostate cancer; green fluorescent protein; cancer biology; angiogenesis; tumor growth.

Paper 10319PRR received Jun. 7, 2010; revised manuscript received Dec. 18, 2010; accepted for publication Dec. 22, 2010; published online Feb. 22, 2011.

1 Introduction

Prostate cancer is an aggressive disease that has high morbidity and mortality rates and is the most commonly diagnosed invasive cancer among men.[1,2] The American Cancer Society estimated that in the United States in 2010 over 215,000 cases would be diagnosed and that over 30,000 men would die of the disease.[3] The current gold standard for prostate cancer detection involves an invasive biopsy, a procedure that contributes to patient discomfort and can have medical complications, such as hemorrhage and infection.[4] Early diagnosis through improved detection would aid in the intervention and treatment of the disease.

The dorsal skin flap window chamber is a well-established model employed in preclinical cancer research. The window chamber facilitates longitudinal studies designed to monitor the tumor microenvironment, track growth, and assess the effects of therapy.[5] It is also compatible with multiple modalities, including fluorescent microscopy,[6–8] nuclear imaging,[9] magnetic resonance,[10–13] electrode imaging,[14] biological polarimetry,[15] pH mapping,[16,17] and computed tomography.[18] However, each of these techniques has limitations related to invasiveness, source of contrast, penetration depth, sensitivity, and/or spatial resolution. To complement existing approaches for studying the tumor environment, we developed a novel *in vivo* platform capable of simultaneous photoacoustic (PA) and pulse echo (PE) imaging of cancer using the mouse window chamber model. In PA imaging, the tissue is illuminated with light, typically in the form of a high-energy pulsed laser. As light penetrates, energy is partially absorbed and converted to heat, causing rapid thermoelastic expansion and generation of ultrasound waves, which are detected to form an ultrasound image.[19] With diffuse illumination, PA imaging provides spatial resolution proportional to the ultrasound wavelength with contrast related to the local optical absorption. Compared to most optical techniques, PA imaging exhibits deeper penetration.[20] Because of the relatively high optical absorption coefficient of hemoglobin, this approach is excellent for characterizing the tumor vasculature and has great potential for noninvasive cancer detection and characterization. Photoacoustic spectroscopy provides additional contrast for identifying different types of tissue and blood vessels based on variations in their optical absorption spectra.[21] On the other hand, PE ultrasound is a well-established technique commonly used for clinical prostate cancer imaging.[22–25] It provides high-resolution anatomical detail related to tissue structure and tumor size. Our imaging platform was designed to simultaneously capture PA and PE signals, producing a dual modality imaging system with contrast related to tumor structure, size, and vasculature. This system is an important enhancement to the window chamber model for monitoring the tumor microenvironment and aiding in the development of novel contrast agents and cancer therapeutics.[26] Finally, dual-modality PA and PE imaging are translational techniques that potentially impact cancer patients, offering complementary contrast and better depth penetration compared to most optical techniques.

Address all correspondence to: Daniel R. Bauer, University of Arizona, Department of Radiology, 1609 N Warren Avenue, Tucson, AZ 85724. Tel: 520-2013;331-2266; E-mail: dan.bauer5@gmail.com.

1083-3668/2011/16(2)/026012/10/$25.00 © 2011 SPIE

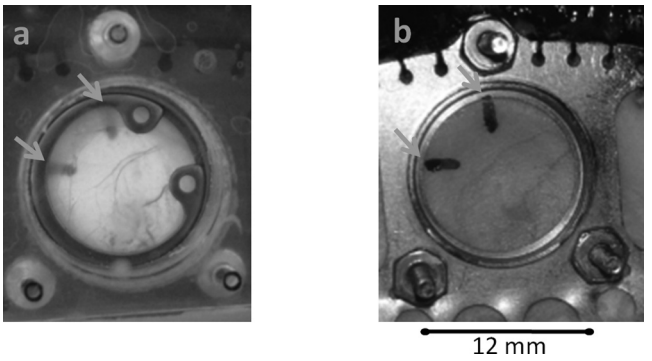

Fig. 1 Photographs of window chamber from mouse R1 on day 9 postimplantation: (a) Photograph from coverslip side and (b) photograph (mirror image) from skin side. The three screws on the chamber were used to secure the window chamber to the imaging apparatus. The arrows denote the fiducial ink mark placed on the skin. The window chamber had a diameter of 12 mm. (Color online only.)

2 Methods and Materials

2.1 *Pulse Echo and Photoacoustic Experimental Setup*

Three severe combined immunodeficient (SCID) mice (R0, R1, R2) were implanted with window chambers. One side of the window chamber had a glass coverslip [referred to as the "coverslip side," Fig. 1(a)], while the other side had exposed skin [referred to as the "skin side," Fig. 1(b)]. PC-3 prostate tumor cells expressing green fluorescent protein (GFP) were implanted into the dorsal skin flap. The subsequent prostate tumor invasions were imaged using multiple modalities over the next four weeks, starting one week after the injection of tumor cells (conforming to protocol). Mice were cared for in accordance with protocols approved by the Institutional Animal Care and Use Committee (IACUC) at the University of Arizona and maintained in a sterile clean-room facility in individual cages with controlled temperature and humidity.

On imaging days, the mice were transported to the laboratory and anesthetized with an isoflurane flow system. A mouse was placed in a gas chamber, and 2% isoflurane was administered using O_2 with a flow rate of ~1 l/min until the mouse was fully anesthetized. The mouse was then moved to the imaging setup, where a spherically focused 25-MHz ultrasound transducer (Olympus V324, Waltham, MA, $f = 12.6$ mm) was placed in a water tank facing the skin side of the mouse separated by a Tegaderm™ acoustic membrane. Hypoallergenic index matching gel (Parker Aquasonic Fairfield, NJ, USA; 100) was placed on the skin side of the window chamber to provide acoustic coupling. The mouse was mounted on a custom-built pad using the three screws, as displayed in Fig. 1(b), to ensure accurate and consistent light delivery onto the window chamber. Anesthesia was maintained with ~1% isoflurane, and Puralube® was placed over the eyes for protection. The body temperature of the mouse was maintained with a heating pad.

A schematic of the PA and PE imaging system is displayed in Fig. 2(a). The 25-MHz focused transducer was connected to a pulser/receiver (Olympus Panametrics Waltham, MA, USA; 5900PR) and placed in a water bath over the mounted window chamber [Fig. 2(b)]. The transducer's focus was positioned between the coverslip and skin surface. The PA setup utilized a tunable pulsed laser source (Continuum Inc., Santa Clara, CA, USA; Surelite I-20, Continuum Inc., 5 ns, ~20 mJ/pulse, tunable 680–1000 nm, 20 Hz) that was synchronized with the data-acquisition system and motor stages (Velmex, Inc. Bloomfield, NY, USA, B100). The laser light passed through a two-lens optical beam expander to increase the beam size to the diameter of the window chamber (12 mm). The beam was passed through a diffuser (not shown) before illuminating the coverslip. A single transmit pulse was synchronized with the laser firing in order to simultaneously capture the PA and PE signals (separated in real time by the one versus two-way travel of the acoustic wave for each modality). The transducer was raster scanned across the window chamber in both lateral dimensions to produce a 3-D data set of the tumor. In general, a rectangular region of interest ($x \approx 6$ mm, $y \approx 14$ mm) was scanned with spacing of $\Delta x = 100$ μm and $\Delta y = 47.6$ μm. The different spacing in the lateral directions is due to the continuous scanning along the y-axis and stepwise

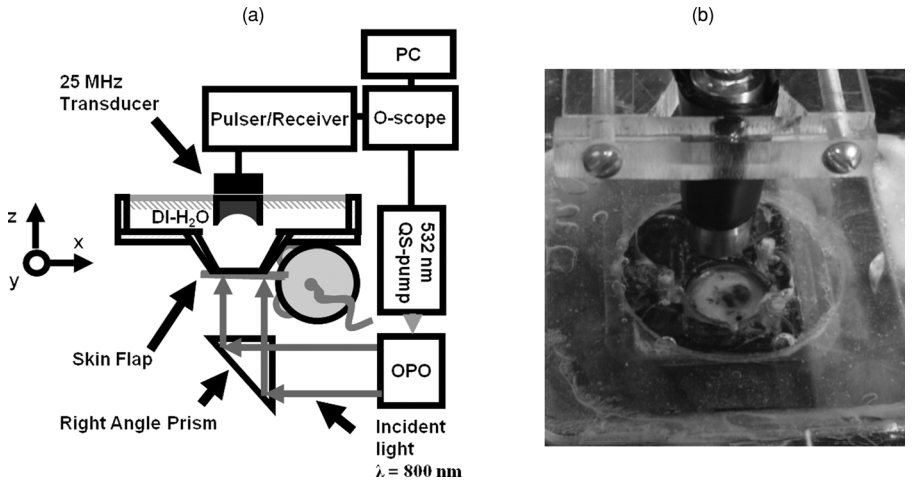

Fig. 2 (a) Diagram of the PA and PE imaging setup. (b) Photograph of the 25-MHz transducer facing the skin side of the window chamber mounted in the water bath. The transducer was raster scanned across the window chamber, while light illuminated the coverslip from below. The synchronization between the laser firing (for PA) and transducer excitation (for PE) enabled simultaneous acquisition.

scanning on the *x*-axis. The transducer was connected via the pulser/receiver to a fast data acquisition board (PDA12, Signatec Inc. Newport Beach CA, USA), and the signal was sampled at 62.5 MHz and digitized at 12 bits. The data were then averaged, filtered, and analyzed in MATLAB® (MathWorks, Inc., Natick, MA).

2.2 *Optical and Fluorescent Imaging Setup*

Optical and fluorescent images of GFP were also captured using high resolution microscopy. Although optical imaging had a limited penetration depth, it provided a reference for comparison to the PE and PA images. A custom plastic holder was also used to fix the mouse using the screws on the window chamber, as depicted in Fig. 1(b). In the same manner as mentioned earlier, mice were anesthetized and the window chamber was fastened to a holder on the microscope stage. Stage clips were used to secure the window chamber in the center of the microscope's field of view. Transillumination images were taken with white light incident on the skin flap. Additionally, fluorescent images of the GFP-expressing tumor cells were captured by illuminating the skin with 488-nm excitation.

2.3 *Data Processing*

The transducer was raster scanned across the window chamber collecting radio frequency (RF) data at each position (i.e., phase and magnitude). Each recorded signal was bandpass filtered between 15 and 30 MHz. The RF data were then demodulated with a Hilbert transform. For spectroscopic scans, the data were scaled to compensate for the wavelength-dependent laser energy output. Individual 2-D slices were then combined into a 3-D data set. A low-order median filter (3 pixels wide) followed by a Gaussian smoothing filter (3–5 pixels wide) were used to improve the signal-to-noise ratio.

As a means to calculate tumor growth using PE data, an automated volume-tracking algorithm utilizing image segmentation was developed, as illustrated in Fig. 3. Each B-mode image was filtered and converted to a binary image using a 50%-of-maximum threshold value. It was difficult to identify tissue interfaces in regions with small PE signals that produced weak boundaries. To compensate for this, each image was filtered with a binary dilation mask, broadening the tissue interface and ensuring a continuous boundary. An erosion filter, the same size and shape as the broadening mask, was then applied to restore the tissue boundary to the approximate original location. After a boundary was established, an automated contour-tracking algorithm was applied to determine the pixel locations of the skin surface and coverslip, which was assumed to be the lower boundary of the skin. The area between the coverslip and skin boundary was then calculated by summing the pixels between these boundaries and multiplying by the known pixel area. Finally, the effective volume of tissue was determined by applying the algorithm to multiple *YZ* planes while taking into account the appropriate interplane distance in the 3-D data set.

An image-segmentation algorithm was also developed to determine the size and track the growth of the fluorescing GFP tumor cells. A user-defined threshold value converted the original fluorescent image into a binary image such that only GFP pixels were thresholded high. The total number of GFP pixels was then calculated. Because the area of the window chamber was known, the area per pixel was used to determine the total number of thresholded pixels, yielding an estimate of the size of the fluorescing tumor.

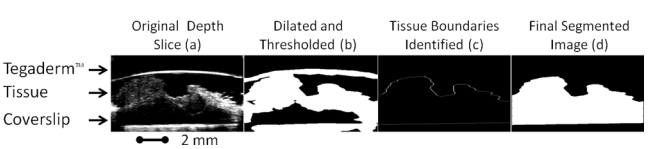

Fig. 3 Graphical representation of PE image segmentation algorithm used to calculate tumor volume: (a) Original PE depth slice (gray, 22 dB) of tumor from mouse R0 on day 23, (b) PE image after filtering, dilation and thresholding, (c) Tegaderm™ and coverslip removed, revealing upper and lower tissue boundaries (edge of coverslip represented the lower tissue boundary), and (d) final segmented image.

3 Results and Discussion

3.1 *Multimodality Imaging*

There are several significant advantages to multimodality imaging because each technique yields different information regarding the tumor microenvironment. When combined with ultrasound imaging, other modalities such as photoacoustic and fluorescent imaging can be useful to further characterize the tumor environment and provide cross-modality comparison and validation.

Fluorescent and optical images of the GFP transfected tumors were used as a standard to track and compare the development of the tumor. Figure 4 depicts a series of images centered on the tumor of mouse R2. The optical image of the window chamber (coverslip side) has been magnified in the transillumination and fluorescent images. The transillumination image describes the tumor environment and nearby vasculature. Two large blood vessels are seen in the vicinity of the tumor, appearing darker than the surrounding tissue. Vessels near the tumor can be imaged for several weeks to enable qualitative analysis of the vascular growth. The fluorescent image of the same region clearly identifies the location of the GFP-expressing tumor cells. The fluorescent images, which represent a 2-D projection of the total fluorescence, reveal the location and concentration of the GFP-labeled tumor cells, and consequently, an estimate of

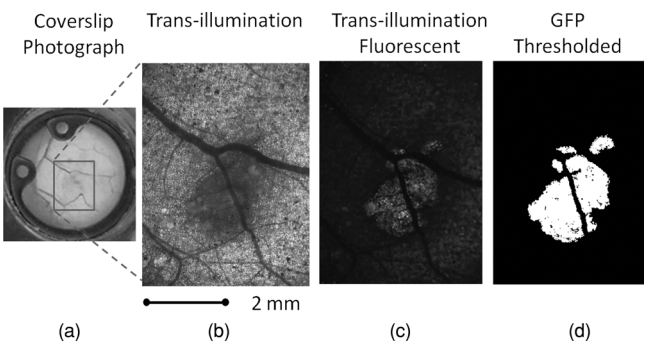

Fig. 4 (Left to Right) Coverslip photograph (day 9); transillumination (day 12); transillumination fluorescent image (day 12); and thresholded GFP fluorescent image (day 12) of mouse R2. Red-scale box has dimensions of approximately 4×6 mm.

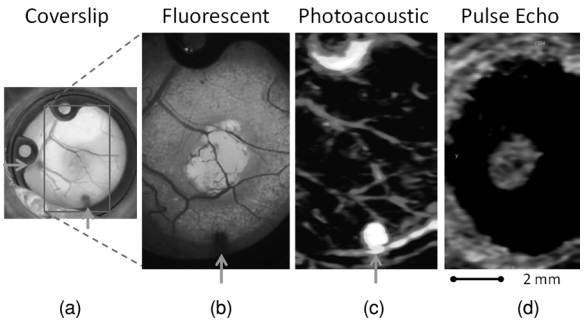

Fig. 5 Example of multimodality images of mouse R2 (Left to Right): Coverslip photograph (day 16), fluorescent image revealing GFP-expressing cells and nearby blood vessels (day 19), maximum projection PA image ($\lambda = 800$ nm, 30 dB, day 16), and lateral PE image of the protruding tumor close to the skin surface (30 dB, day 16). Each modality provides different contrast and spatial detail. Location of GFP is revealed in fluorescent image, blood vessel locations are displayed in PA image, and the tumor's depth profile and physical structure are displayed in the PE image. The arrows denote the fiducial ink mark placed on the skin. Scale box has dimensions of 6×11 mm. (Color online only.)

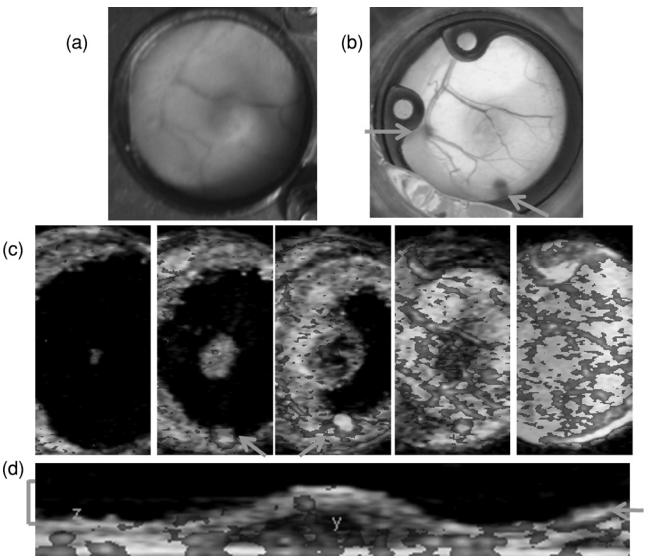

Fig. 6 Optical, PA and PE images from tumor invasion of mouse R2 on day 16. Photographs (6×6 mm) of window chamber's (a) skin side and (b) coverslip side. (c) Series of superimposed PA (hot, $\lambda = 800$ nm, 20 dB) and PE (gray, 35 dB) slices (*XY* planes, 6×12 mm) stepping in the depth direction (Δz between slices = 240 μm). (d) *YZ* slice center of tumor (8×1.25 mm); bracket denotes range of slices in (c). The arrows indicate the common ink mark. (Color online only.)

the lateral tumor size. In each image, the vasculature, size, and location of the tumor can be distinguished. The automated fluorescent thresholding algorithm, demonstrated in Fig. 4, was used to calculate the size of the fluorescing tumor.

A photograph of the coverslip with the associated fluorescent, PA, and PE images of mouse R2 is displayed in Fig. 5. The photograph indicates that the tumor (middle of the red-scale box) is slightly darker than the surrounding healthy tissue. The fluorescent, PA, and PE images complement each other and reveal different sources of contrast related to the tumor environment. The transillumination fluorescent image portrays several blood vessels and the fluorescing tumor cells. The same blood vessels are resolved using PA imaging because blood has a higher optical absorption at 700 nm than surrounding tissue.[27] Whereas the optical and fluorescent images are 2-D projections of the tumor and surrounding tissue, the PA image provides depth information, so that the location of blood vessels can be imaged in three dimensions. The maximum intensity projection along the depth direction of the PA signal is presented in Fig. 5. This perspective enables a direct comparison between the 3-D PA data and the 2-D fluorescent images. In the PA image, blood vessels are clearly detected and consistent with the vasculature depicted in the optical images. Additionally, the PA signal has the added benefit of mapping blood vessels deep under the skin surface (>1 cm), which cannot normally be resolved using such optical techniques as confocal microscopy and optical coherence tomography.[28]

The PE image in Fig. 5 provides additional information regarding the physical characteristics of the tumor, such as size, shape, and echogenicity. This structural information supplements the information provided by the other modalities. In this example, the PE image (*XY* plane near top of the tumor) provides depth information not available in the fluorescent image and illustrates the tumor protruding outward toward the skin surface in the region of the GFP signal. The center of the tumor appears relatively homogeneous at this position. Thus, PA and PE imaging offer complementary contrast related to the cancerous microenvironment and vascular network during the tumor invasion. A dual-modality system capable of PA and PE imaging could be a valuable tool in the clinic for cancer diagnostics or monitoring therapy.

3.2 *Combined Pulse Echo and Photoacoustic Imaging*

Coregistered and superimposed PA (hot) and PE (gray) images are presented in Fig. 6 for mouse R2 on day 16. Figure 6(c) depicts *XY* planes (from left to right), starting at the top of the tumor and progressing downward with a depth spacing of 240 μm. In the first image, the top of the tumor and window chamber border can be seen. Progressively deeper *XY* lateral planes show that the tumor appears to be reasonably circular, a claim that is validated by the skin-side photograph of the window chamber from Fig. 6(a). Also, the tumor protrudes outward (away from the skin) slightly ($\approx$700 μm) as estimated from the PE data from Fig. 6(d).

The second image in Fig. 6(c) displays the size of the tumor increasing downward and large fiducial ink mark placed on the skin (denoted with arrow). The ensuing planes inside the tumor reveal the 3-D vascular network. The blood vessels displayed in the PA image are well correlated with the photographs of the window chamber from Fig. 6. Because PA imaging has better depth penetration than traditional optical techniques, the depth location of the blood vessels can be determined. For comparison, the *YZ* profile image of the tumor is depicted in Fig. 6(d) with the bracket indicating the range of lateral planes presented in Fig. 6(c). Note that the fiducial mark placed on the skin is localized to the top of the skin and not visualized in deeper planes.

A series of optical and PE images from mouse R2 on day 23 are presented in Fig. 7. The photographs in Figs. 7(a) and 7(b)

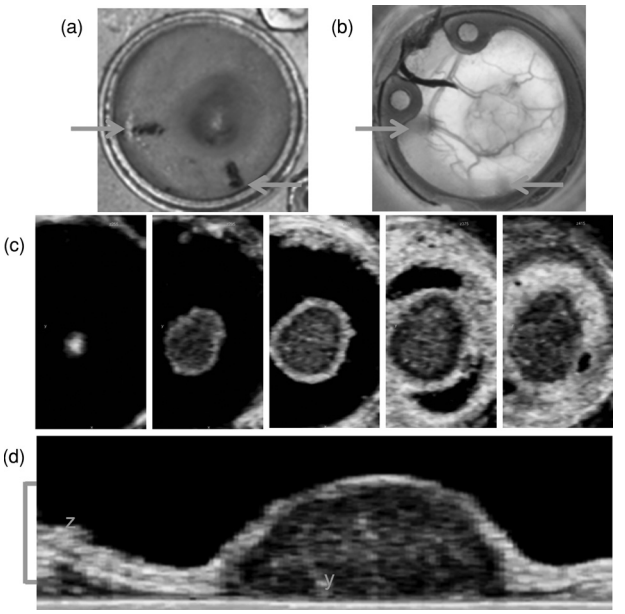

Fig. 7 Optical and PE images from mouse R2 on day 23. Photographs (6×6 mm) of window chamber's (a) skin side and (b) coverslip side. (c) Series of lateral PE slices (35 dB) stepping in the depth direction (Δz between slices = 480 μm). (d) *YZ* slice through same tumor (10×3 mm); bracket denotes range of slices in (c). The arrows indicate the common ink mark. (Color online only.)

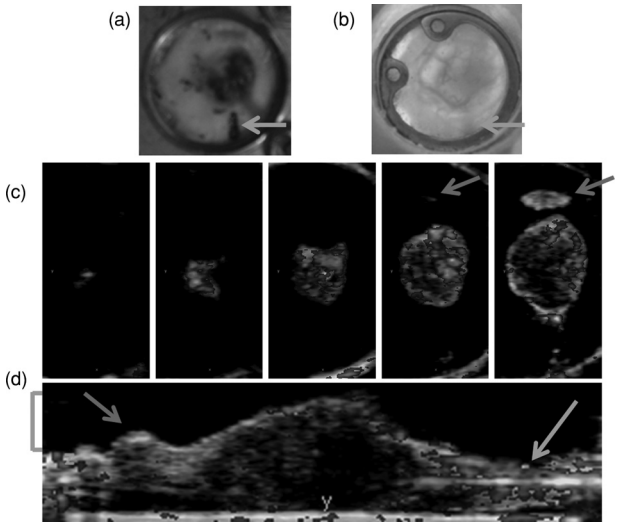

Fig. 8 Optical, PA, and PE images from the tumor invasion of mouse R2 on day 29. Photographs (6×6 mm) of window chamber's (a) skin side and (b) coverslip side. (c) Series of superimposed PA (hot, $\lambda = 800$ nm, 25 dB) and PE (gray, 35 dB) slices (*XY* planes, 6×12 mm) stepping in the depth direction (Δz between slices = 240 μm). (d) *YZ* slice through the center of the tumor (12×3 mm); bracket denotes range of slices in (c). Primary sources of the PA signal were the hemorrhage visible from the skin-side photograph and the common ink mark, denoted in (d) by right arrows. Left arrow in (d) indicates tumor side-lobe. (Color online only.)

reveal the circular shape of the tumor, which is consistent with the images from day 16 (see Fig. 6), except that the tumor has grown laterally. These optical images, however, provide minimal depth information. On the other hand, a sequence of PE images [Figs. 7(c) and 7(d)] demonstrates the imaging capability of 3-D high-resolution ultrasound for capturing depth information and characterizing the tumor structure, size, and echogenicity. Images reveal a bright, hyperechoic outer ring around the tumor, and a dark, hypoechoic tumor core. The reduced PE signal in the tumor's center, suggests a developing necrotic core, as commonly seen in cancerous tumors.[18,29,30] A dense fibrous outer ring has been previously associated with cancer progression.[18,31] These images characterize the 3-D shape and size of the tumor as it protrudes outward away from the skin. By day 23, the tumor extended well beyond the original boundary of the skin by >2 mm.

On day 29, the tumor continued to protrude outward by approximately the same amount as the previous week (∼2 mm). However, the tumor's shape and overall profile had changed considerably. For instance, the left side of the window chamber developed a small tumor side lobe [Fig. 8(d); left arrow]. A large portion of the necrotic core is hypoechoic, indicating a region of uniform density and low scattering, such as a localized region of fluid.[32,33] In addition, the tumor of mouse R2 experienced a substantial hemorrhage in the final week of the study [Fig. 8(a)]. Because dried coagulated blood is a strong optical absorber,[34] we expected PA imaging to be able to map the hemorrhage. As displayed in both the photographs and PA images in Fig. 8, the top of the tumor endured considerable hemorrhage. Despite light entering the window chamber through the coverslip, PA imaging was still able to detect the hemorrhage at the opposite side of the chamber near the skin surface with excellent signal-to-noise ratio (>20 dB). This illustrates that 3-D PA imaging has adequate depth penetration for imaging the entire extent of the window chamber. The strong PA signals in Fig. 8 are primarily due to the coagulated blood and fiducial ink mark. Hemorrhaging has previously been associated with prostate cancer.[32,35] It is possible that the rigid coverslip and rapid growth of the prostate tumor–induced excessive stress at the skin surface, causing blood vessels to rupture. Alternatively, the hemorrhage may have also been caused by rapid angiogenesis and resulting collapse of the hemorrhage-prone blood vessels near the tumor.[36]

3.3 *Photoacoustic Imaging During Cancer Progression*

Photoacoustic imaging was used over the course of the study to monitor the 3-D optical absorption of the tumor microenvironment. The PA maximum intensity projections for mouse R2 are displayed in Fig. 9. The PA images of the vascular network from days 9 and 16 are consistent with the optical images, but also provide additional depth information. For example, in the PA images on day 16, blood vessels were not visible in the skin-side photograph; however, these blood vessels were detected using PA imaging [Fig. 9; small arrows]. There also appears to be an increase in vasculature growth near the center of the tumor from day 9 to 16. This suggests the presence of angiogenesis, which is commonly associated with prostate cancer progression.[37] Because in this study we did not measure blood volume fraction or molecular markers of angiogenesis, we can only speculate on neovascularization. On day 29, the PA signal is clearly dominated by the hemorrhage and ink mark placed on the skin of the mouse. Individual blood vessels are no longer visible, although

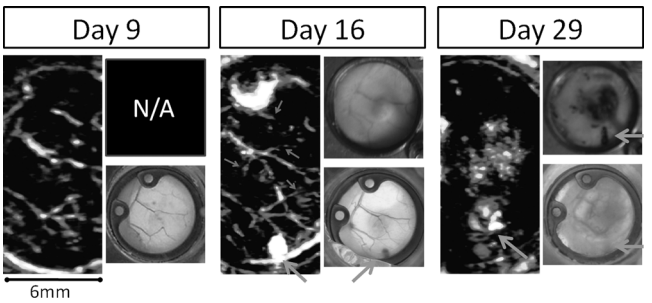

Fig. 9 Optical and PA tumor progression for mouse R2. (left) Photoacoustic maximum intensity projection ($\lambda = 800$ nm, 6×12 mm). Photographs (6×6 mm) of window chamber's skin side (top right) and coverslip side (bottom right). PA images on days 9 and 16 revealed a map and progression of the vascular network. The PA signal for day 29 is largely dominated by the extensive hemorrhage, which is consistent with the skin side photograph. On day 16, several blood vessels were resolved using photoacoustics (labeled with small arrows), but not visualized in the skin side photograph. The large arrows denote the fiducial ink mark. (Color online only.)

the optical and maximum projection PA images are strongly correlated. Hemorrhaging is not unexpected in a tumor with a nutrient deficient core that is weak and necrotic.[33,38–40] Thus, 3-D PA imaging of the tumor environment was consistent with the optical and fluorescent images and provided additional depth resolution [see Fig. 8(d)].

3.4 *Pulse Echo Imaging during Cancer Progression*

The segmentation algorithm described in Sec. 2.3 was used to estimate the tumor size and growth rate based on fluorescent and PE images. The fluorescent images convey the distribution of GFP-expressing tumor cells. Although only 2-D projections, they represent the gold standard for determining size, shape, and growth rate specific to the tumor. Figure 10 (left) depicts the lateral growth of the tumor during three weeks or more of fluorescent imaging. Serial fluorescent images from one mouse are displayed in Fig. 10 (right). Using the GFP thresholding algorithm, the area of each mouse tumor was calculated three

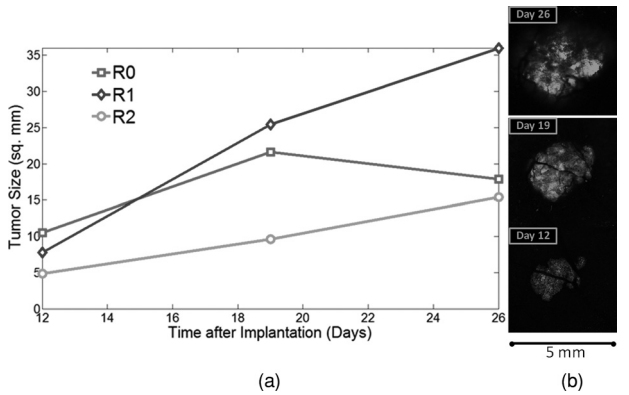

Fig. 10 (left) Tumor size and growth for three mice based on fluorescent GFP segmentation algorithm. Tumor cells were implanted on day 0. Average growth rates for the mice (R0, R1, R2), determined by the slope of the best fit line, were 0.52, 2.02, and 0.75 mm^2/day. (right) Time serial fluorescent images of GFP in mouse R2's tumor spanning a 5×5 mm region of interest.

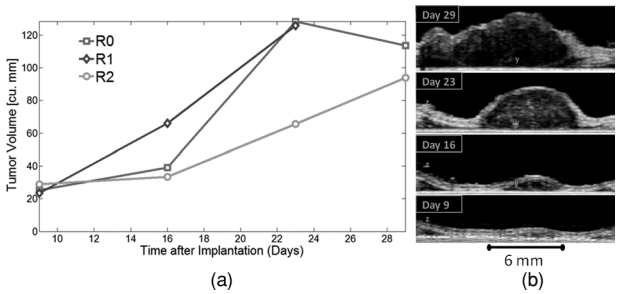

Fig. 11 (left) Volumetric tissue growth for all three mice based on the PE segmentation algorithm. No data point was available for mouse R1 on day 29, because the mouse died prematurely. Day 0 corresponds to the day tumor cells were implanted. Average growth rates for the mice based on the slope of the best fit line were 5.35, 7.32, and 3.37 mm^3/day. (right) Time serial PE (gray, 35 dB) depth images at the approximate center of mouse R2's tumor (*YZ* planes), illustrating tumor growth and proliferation. PE images were part of a 3-D data set.

times with seven-day intervals between fluorescent images. For each animal, average growth rates were calculated based on the slope of the best-fit line. Two mice (R1 and R2) exhibited a monotonic increase in tumor area with average respective growth rates of 2.02 and 0.75 mm^2/day. The third tumor (R0) decreased slightly in size during the last week of the study, but still had an average growth rate of 0.52 mm^2/day.

Three-dimensional high-fresolution PE images were also analyzed to determine volumetric tissue growth. Results are summarized in Fig. 11. It was assumed that most of the increase in volume was attributed to tumor growth or a resulting by-product, such as edema or inflammation.[41] As expected, all three mice demonstrated a general increase in tissue volume over the course of the experiment, with average growth rates of 5.35, 7.32, and 3.37 mm^3/day for mouse R0, R1, and R2, respectively. It should also be noted that all three mice exhibited a faster rate of tumor growth after day 16. Figure 11 (right) displays an example of tumor growth and proliferation based on PE images through the center of mouse R2's tumor. The smaller growth rate in R2's tumor from day 9 to 16 appeared to be in agreement with the tumor cross section from the associated days. The dramatic increase in tumor size between days 16 and 29 was also consistent with the associated depth profiles of the tumor. As with the fluorescent data, the tumor volume increased monotonically at all time points, except for mouse R0's tumor during the last week of imaging. This result was consistent with fluorescent imaging.

Normalized tumor growth based on fluorescent and PE image segmentation is plotted together in Fig. 12 with each data set scaled to its initial value. The linear correlation coefficients for the calculated tumor growth based on the PE and fluorescent images are also provided. Results from all three mice demonstrated significant positive correlation coefficients ($R = 0.662$, 0.990, 0.992). An average correlation coefficient ($R = 0.97$) and confidence interval ($p < 0.01$) were calculated using a Fisher z-transform and a bootstrapping algorithm with randomized shuffling (>1000) of the original data.[42,43] It should be noted that the tumor's growth is impeded laterally by the window chamber and axially by the coverslip, and, thus growth was not expected to be uniform in all directions due to these boundary restrictions. Although direct comparisons between the lateral GFP distribution and tissue volume was difficult, this approach

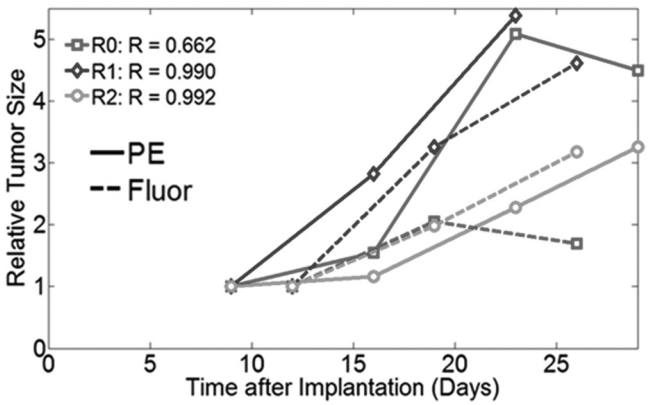

Fig. 12 Tumor growth determined from PE (solid lines) and fluorescent (dashed lines) segmentation algorithms. Measurements for each modality were normalized to their respective initial values. Correlation coefficients for each mouse between the pulse echo and fluorescent tumor size measurements are also indicated. A Fisher *z*-transform and bootstrapping algorithm indicated that the growth curves obtained by PE and fluorescent imaging were highly correlated and significant ($R_{avg} = 0.97$, $p < 0.01$).

provided cross-validation between the tumor volume tracking results and those from the fluorescent images. For example, mouse R0 exhibited a reduction in both tumor area and volume over the last week of the study. Although this resulted in a reduced linear correlation coefficient ($R = 0.662$), both imaging approaches produced the same result, which added confidence to the measurement. There were several plausible explanations for the apparent decrease in tumor size. The optical and fluorescent images for mouse R0 indicated that it proliferated toward the edge of the window chamber, such that by day 29, it extended to the chamber boundary. Therefore, the tumor may have extended beyond the window chamber, so that the calculated volume was not accurate. This outcome could also be explained by the mouse's own immune system fighting off the tumor cells or reduced edema.[44] In general, the fluorescent area and tumor volume measurements are strongly correlated, both appearing to be acceptable methods for tracking tumor growth. Pulse echo imaging, however, provides additional depth information regarding tumor progression.

3.5 *Photoacoustic Spectroscopy*

Spectroscopic photoacoustic imaging enables noninvasive detection and mapping of the wavelength-dependent optical absorption of tissue and contrast agents. Because the optical absorption spectra of hemoglobin is highly dependent on the presence of oxygen,[19] PA spectroscopy can be used to detect relative and absolute levels of blood oxygen saturation.[45–48] This can be useful in cancer imaging to distinguish veins from arteries or identify hypoxic regions near a tumor.[49,50] In previous sections, we demonstrated that PA imaging was a valuable tool to identify and track blood vessels and hemorrhage in the tumor environment. We now revisit one data set and apply PA spectroscopy to characterize relative blood oxygen saturation in the imaged blood vessels. Because of slow scanning of the mechanical system, we limited PA spectroscopy to a single B-mode image at each laser wavelength (680–900 nm, $\Delta\lambda = 25$ nm). In this section, we calculated the slope of the best-fit line at each pixel between the PA signal magnitude and incident laser wavelength.[51,52] The derivative of the PA signal is dependent on the localized optical absorption coefficient of the tissue and thus an indicator of a blood vessel's degree of oxygen saturation.[53] Figure 13(a) demonstrates a series of PA images in the window chamber at multiple laser wavelengths. Figure 13(c) represents a spectroscopic PA image, where the color (hot/cold) at each pixel denotes the sign and magnitude of the PA signal's

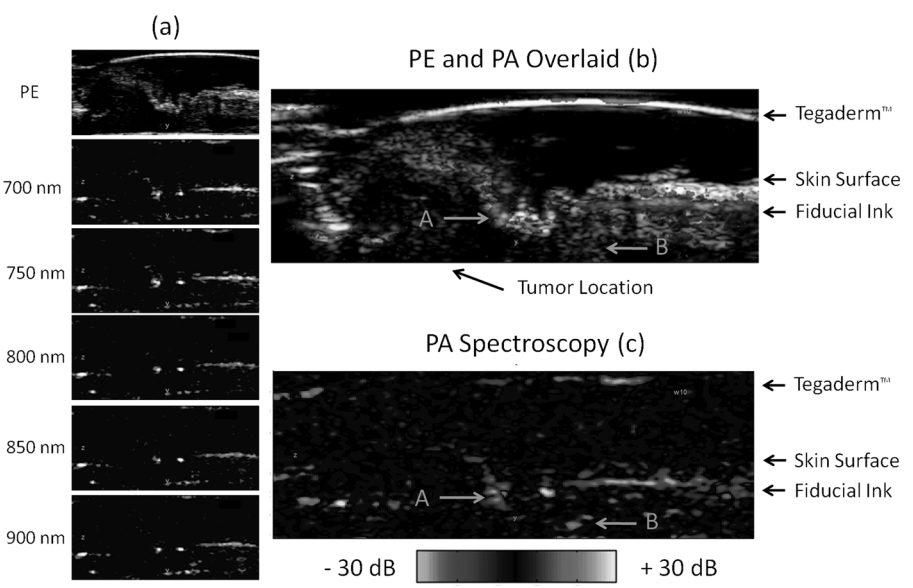

Fig. 13 Spectroscopic PA imaging of mouse R0 on day 29: (a) PA images (20 dB) labeled with incident laser wavelength, (b) PA image (hot, $\lambda = 800$ nm, 20 dB) superimposed on co-registered PE image (gray, 35 dB), and (c) Spectroscopic PA image with color (hot/cold) representing the magnitude of the slope of the PA signal with laser wavelength. The magnitude of the slope has been compressed and displayed with a 30-dB dynamic range. Variation in blood oxygen saturation is a likely contributor to the different slopes. The PA slope at each pixel was determined from the best linear fit (see Fig. 14 for examples at regions A and B). All images have dimensions of 10×4.5 mm.

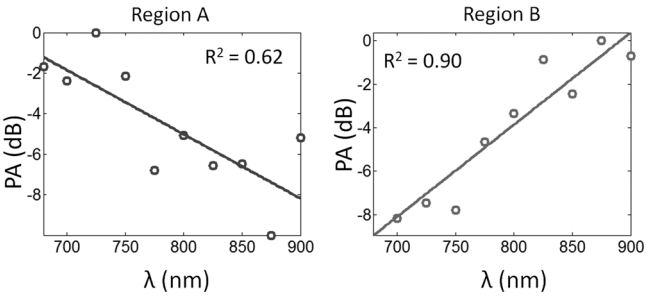

Fig. 14 Magnitude of the PA signal versus laser wavelength for regions A and B from Fig. 13(c). The slope of the best-fit line for region A (–0.032 dB/nm) and B (0.042 dB/nm) were consistent with the optical absorption spectrum of deoxygenated and oxygenated hemoglobin, respectively. However, there were other possible contributors to the wavelength dependence of the PA signal (see text).

slope between 680 and 900 nm. The magnitude of the slope is displayed on a decibel scale with a 30-dB dynamic range. Two small regions of interest are marked A and B for further analysis. Figure 13(b) displays the PA signal at 800 nm (hot) superimposed on the coregistered PE image (gray).

Figure 14 depicts the magnitude of the PA signal as a function of wavelength at two regions of interest indicated in Fig. 13(c). The slope of the photoacoustic spectrum at region A is consistent with the absorption spectrum of deoxygenated hemoglobin, while the spectrum of region B is consistent with oxygenated hemoglobin.[19] However, there are other factors that might contribute to the wavelength dependence of the PA signal. For example, the PA signal is affected by laser fluence at each pixel location. Fluence depends primarily on the incident energy and illumination pattern, as well as the absorption and scattering coefficients spanning the complete optical path of all photons that reach that pixel location. Because the optical properties of the tissue were not known at each position inside the window chamber, Monte Carlo simulations could not be used to accurately estimate the magnitude of these effects at each wavelength. Instead, we used estimates of these contributing factors, revealing that these effects by themselves cannot explain the relative difference, nearly an order of magnitude that was observed in the spectroscopic PA signal between 680 and 900 nm. First, we used broad and diffuse light delivery through the coverslip such that the illumination pattern was similar entering the tissue at each wavelength. Second, our estimates of light loss due to scattering and attenuation differences in soft tissue were much smaller than the observed variation in the PA signal at each wavelength. For example, at 800 nm, blood has a much larger absorption coefficient ($\sim$2.0 cm^{-1}) than surrounding tissue.[19,48,54] The attenuation coefficient of extravascular tissue ($\sim$0.2 cm^{-1}) in the window chamber in the near infrared is at least an order of magnitude less.[55,56] Given the diameter of a typical large blood vessel in the chamber ($\sim$100 μm), this equates to a total attenuation of $<$2.0%. Moreover, the effect on the wavelength dependent absorption, as suggested by the slope calculation, was expected to be less. Combined with the small geometrical path difference between regions A and B of $\sim$500 μm, we are confident that the wavelength-dependent loss due to differences in the laser fluence at each pixel was $<$5%, far less than the observed difference in the wavelength-dependent slope of the PA signal. Therefore, while incremental light scattering and absorption of tissue unquestionably plays a role in the final absorption spectrum described by the spectroscopic PA signal, we estimated this effect to be minor compared to observed differences in the PA signal presented in Figs. 13 and 14. This further supports PA spectroscopy as a tool for classifying blood vessels according to their oxygen content. This can be especially valuable for imaging prostate and other aggressive tumors that are often associated with hypoxic regions and reduced blood oxygen levels.[57–59] Thus, PA imaging and spectroscopy is not only a powerful technique for mapping the vascular network inside the window chamber, but also for monitoring blood oxygen saturation in the tumor microenvironment. PA spectroscopy can be extended to track absorbing contrast agents with high specificity.[26,60,61]

3.6 *Future Considerations and Implications for Cancer Patients*

The window chamber offers multimodality imaging in a well-controlled *in vivo* setting. This is an ideal environment to develop new imaging technology and targeted contrast agents for detecting molecular indicators for diagnostic and prognostic imaging of cancer.[26,62–65] The mouse window chamber model also enables testing novel cancer therapies using several modalities for comparison and cross-validation. First-stage screening of new drugs potentially accelerates their translation to cancer patients. The dual-modality system described in this study provides additional functionality and contrast for studying the tumor microenvironment using the window-chamber model. Photoacoustic imaging also overcomes penetration limits of traditional optical techniques. This suggests that an optimized PE and PA imaging system designed for humans might offer unique attributes for cancer imaging and monitoring therapy. Early clinical studies using PA for breast imaging demonstrate some of these advantages.[66,67] The light delivery system employed in this study could be further adapted for reflection mode PA imaging using an in-line acoustic reflector with a single element[68] or clinical array transducer.[64] Such a handheld system would be capable of noninvasive imaging through the skin of humans (or small animals) for dual-modality PA and PE imaging of cancer growth, tumor vasculature, angiogenesis, and blood oxygen saturation. Combined with molecular contrast agents, a real-time PE and PA imaging system might aid in the diagnosis and prognosis of prostate and other types of cancer and provide feedback during therapy.

4 Conclusion

We described a novel, high-resolution, dual-modality imaging system that complements traditional approaches for tracking cancer progression using the mouse window-chamber model. The platform provides alternative sources of contrast and enhanced depth resolution compared to other techniques often applied to the window chamber model. Three-dimensional imaging of prostate tumor invasions revealed dramatic growth, blood vessels, and hemorrhaging several millimeters from the coverslip. These observations complemented fluorescent imaging of GFP in the window chamber. The combined platform is ideally suited for optimizing PA imaging and molecular contrast agents for advanced diagnosis and prognosis of prostate

and other types of cancer. Translation of these technologies to the clinic could potentially have a profound impact on novel detection and treatment of prostate cancer.

Acknowledgments

The authors acknowledge support from the Arizona Cancer Center Seed Grant Nos. IRG-7400128 and NSF 0853618, Advanced Research Institute for Biomedical Imaging, Technology and Research Initiative Funding, and the National Institutes of Health. Special thanks is extended to Christy Howison, Gillian D. Paine-Murrieta, Michael Bernas, Bethany Skovan, and the Experimental Mouse Shared Service for aiding in animal preparation. We also extend thanks to Art Gmitro's Biomedical Imaging Laboratory for assistance with fluorescent imaging.

References

1. K. L. Meehan, J. W. Holland, and H. J. S. Dawkins, "Proteomic analysis of normal and malignant prostate tissue to identify novel proteins lost in cancer," *Prostate* **50**(1), 54–63 (2002).
2. L. K. Dennis and M. I. Resnick, "Analysis of recent trends in prostate cancer incidence and mortality," *Prostate* **42**(4), 247–252 (2000).
3. A. Jemal, R. Siegel, J. Xu, and E. Ward, "Cancer statistics, 2010," *CA Cancer J. Clin.* **60**(5), 277 (2010).
4. M. H. Kawachi, R. R. Bahnson, M. Barry, J. E. Busby, P. R. Carroll, H. B. Carter, W. J. Catalona, M. S. Cookson, J. I. Epstein, R. B. Etzioni, V. N. Giri, G. P. Hemstreet, R. J. Howe, P. H. Lange, H. Lilja, K. R. Loughlin, J. Mohler, J. Moul, R. B. Nadler, S. G. Patterson, J. C. Presti, A. M. Stroup, R. Wake, and J. T. Wei, "Prostate cancer early detection," *J. Natl. Comprehens. Cancer Netw.* **8**(2), 240–262 (2010).
5. D. R. Bauer, R. Olafsson, L. G. Montilla and R. S. Witte, "*In vivo* multi-modality photoacoustic and pulse echo tracking of prostate tumor growth using a window chamber," *Proc. SPIE* **7564**, 75643B (2010).
6. D. E. Meyer, G. A. Kong, M. W. Dewhirst, M. R. Zalutsky, and A. Chilkoti, "Targeting a genetically engineered elastin-like polypeptide to solid tumors by local hyperthermia," *Cancer Res.* **61**(4), 1548–1554 (2001).
7. G. Helmlinger, F. Yuan, M. Dellian, and R. K. Jain, "Interstitial pH and pO2 gradients in solid tumors *in vivo*: high-resolution measurements reveal a lack of correlation," *Nat. Med.* **3**(2), 177–182 (1997).
8. P. Oh, P. Borgstrom, H. Witkiewicz, Y. Li, B. J. Borgstrom, A. Chrastina, K. Iwata, K. R. Zinn, R. Baldwin, J. E. Testa, and J. E. Schnitzer, "Live dynamic imaging of caveolae pumping targeted antibody rapidly and specifically across endothelium in the lung," *Nat. Biotechnol.* **25**(3), 327–337 (2007).
9. L. Y. Chen, L. S. Gobar, N. G. Knowles, D. W. Wilson, and H. H. Barrett, "Direct charged-particle imaging system using an ultra-thin phosphor: physical characterization and dynamic applications," *IEEE Trans. Nucl. Sci.* **56**(5), 2628–2635 (2009).
10. M. W. Dewhirst, E. T. Ong, R. D. Braun, B. Smith, B. Klitzman, S. M. Evans, and D. Wilson, "Quantification of longitudinal tissue pO2 gradients in window chamber tumours: impact on tumour hypoxia," *Br. J. Cancer* **79**(11–12), 1717–1722 (1999).
11. K. Erickson, R. A. Braun, D. H. Yu, J. Lanzen, D. Wilson, D. M. Brizel, T. W. Secomb, J. E. Biaglow, and M. W. Dewhirst, "Effect of longitudinal oxygen gradients on effectiveness of manipulation of tumor oxygenation," *Cancer Res.* **63**(15), 4705–4712 (2003).
12. L. Yuxiang, M. F. S. Salek, N. Jennings, and A. F. Gmitro, "An optical imaging system for window chambers in Mri System," *Proc. SPIE* **6849**, 684907 (2008).
13. A. F. Gmitro, Y. Lin, and M. F. Salek, "A system for multi-modality optical and MR imaging of implanted window chambers," in *Novel Techniques in Microscopy*, OSA Tech. Digest, Vancouver (2009).
14. M. W. Dewhirst, E. T. Ong, B. Klitzman, T. W. Secomb, R. Z. Vinuya, R. Dodge, D. Brizel, and J. F. Gross, "Perivascular oxygen tensions in a transplantable mammary tumor growing in a dorsal flap window chamber," *Radiat. Res.* **130**(2), 171–182 (1992).
15. M. F. G. Wood, N. Ghosh, M. A. Wallenburg, E. H. Moriyama, S.-H. Li, R. D. Weisel, B. C. Wilson, R.-K. Li, and I. A. Vitkin, "Turbid polarimetry for tissue characterization," *Proc. SPIE* **7371**, 737106 (2009).
16. R. A. Gatenby, E. T. Gawlinski, A. F. Gmitro, B. Kaylor, and R. J. Gillies, "Acid-mediated tumor invasion: a multidisciplinary study," *Cancer Res.* **66**(10), 5216–5223 (2006).
17. I. F. Robey, B. K. Baggett, N. D. Kirkpatrick, D. J. Roe, J. Dosescu, B. F. Sloane, A. I. Hashim, D. L. Morse, N. Raghunand, R. A. Gatenby, and R. J. Gillies, "Bicarbonate increases tumor ph and inhibits spontaneous metastases," *Cancer Res.* **69**(6), 2260–2268 (2009).
18. J. E. Chomas, R. E. Pollard, A. R. Sadlowski, S. M. Griffey, E. R. Wisner, and K. W. Ferrara, "Contrast-enhanced US of microcirculation of superficially implanted tumors in rats," *Radiology* **229**(2), 439–446 (2003).
19. D. J. Faber, E. G. Mik, M. C. G. Aalders, and T. G. van Leeuwen, "Light absorption of (oxy-)hemoglobin assessed by spectroscopic optical coherence tomography," *Opt. Lett.* **28**(16), 1436–1438 (2003).
20. P. C. Beard and T. N. Mills, "2D line-scan photoacoustic imaging of absorbers in a scattering tissue phantom," *Proc. SPIE* **4256**, 34–42 (2001).
21. J. Laufer, D. Delpy, C. Elwell, and P. Beard, "Quantitative spatially resolved measurement of tissue chromophore concentrations using photoacoustic spectroscopy: application to the measurement of blood oxygenation and haemoglobin concentration," *Phys. Med. Biol.* **52**(1), 141–168 (2007).
22. A. Athanasiou and A. Tardivon, "Ultrasound elastography in cancer imaging: principles and current applications," *Oncologie* **12**(3), 208–212 (2010).
23. T. Ripert, M. D. Azemar, J. Menard, Y. Bayoud, R. Messaoudi, F. Duval, and F. Staerman, "Transrectal high-intensity focused ultrasound (HIFU) treatment of localized prostate cancer: review of technical incidents and morbidity after 5 years of use," *Prostate Cancer Prostat. Dis.* **13**(2), 132–137 (2010).
24. V. V. Iremashvili, A. K. Chepurov, K. M. Kobaladze, and S. I. Gamidov, "Periprostatic local anesthesia with pudendal block for transperineal ultrasound-guided prostate biopsy: a randomized trial," *Urology* **75**(5), 1023–1027 (2010).
25. L. Solorio, B. M. Babin, R. B. Patel, J. Mach, N. Azar, and A. A. Exner, "Noninvasive characterization of *in situ* forming implants using diagnostic ultrasound," *J. Control. Release* **143**(2), 183–190 (2010).
26. R. Olafsson, D. R. Bauer, L. G. Montilla, and R. S. Witte, "Real-time, contrast enhanced photoacoustic imaging of cancer in a mouse window chamber," *Opt. Express* **18**(18), 18625–18632 (2010).
27. A. Roggan, M. Friebel, K. Dorschel, A. Hahn, and G. Muller, "Optical properties of circulating human blood in the wavelength range 400–2500 nm," *J. Biomed. Opt.* **4**(1), 36–46 (1999).
28. H. F. Zhang, K. Maslov, G. Stoica, and L. H. V. Wang, "Functional photoacoustic microscopy for high-resolution and noninvasive *in vivo* imaging," *Nat. Biotechnol.* **24**(7), 848–851 (2006).
29. L. Bingle, C. E. Lewis, K. P. Corke, M. W. R. Reed, and N. J. Brown, "Macrophages promote angiogenesis in human breast tumour spheroids *in vivo*," *Br. J. Cancer* **94**(1), 101–107 (2005).
30. M. W. Dewhirst, E. J. Ozimek, J. Gross, and T. C. Cetas, "Will hyperthermia conquer the elusive hypoxic cell? Implications of heat effects on tumor and normal-tissue microcirculation," *Radiology* **137**(3), 811–817 (1980).
31. R. K. Karls, J. Guarner, D. N. McMurray, K. A. Birkness, and F. D. Quinn, "Examination of Mycobacterium tuberculosis sigma factor mutants using low-dose aerosol infection of guinea pigs suggests a role for SigC in pathogenesis," *Microbiology* **152**(6), 1591–1600 (2006).
32. X. Zhou, B. W. Pogue, B. Chen, and T. Hasan, "Analysis of effective molecular diffusion rates for verteporfin in subcutaneous versus orthotopic dunning prostate tumors," *Photochem. Photobiol.* **79**(4), 323–331 (2009).
33. L. T. Baxter and R. K. Jain, "Transport of fluid and macromolecules in tumors. II. Role of heterogeneous perfusion and lymphatics," *Microvasc. Res.* **40**(2), 246–263 (1990).
34. R. J. Talbert, S. H. Holan, and J. A. Viator, "Photoacoustic discrimination of viable and thermally coagulated blood using a two-wavelength

method for burn injury monitoring," *Phys. Med. Biol.* **52**(7), 1815–1829 (2007).
35. S. Shan, N. D. Robson, Y. Cao, T. Qiao, C. Y. Li, C. D. Kontos, M. Garcia-Blanco, and M. W. Dewhirst, "Responses of vascular endothelial cells to angiogenic signaling are important for tumor cell survival," *FASEB J.* (2003).
36. G. M. Tozer, S. Akerman, N. A. Cross, P. R. Barber, M. A. Bjorndahl, O. Greco, S. Harris, S. A. Hill, D. J. Honess, C. R. Ireson, K. L. Pettyjohn, V. E. Prise, C. C. Reyes-Aldasoro, C. Ruhrberg, D. T. Shima, and C. Kanthou, "Blood vessel maturation and response to vascular-disrupting therapy in single vascular endothelial growth factor-A isoform-producing tumors," *Cancer Res.* **68**(7), 2301–2311 (2008).
37. H. Zhong, K. Chiles, D. Feldser, E. Laughner, C. Hanrahan, M. M. Georgescu, J. W. Simons, and G. L. Semenza, "Modulation of hypoxia-inducible factor 1 alpha expression by the epidermal growth factor/phosphatidylinositol 3-kinase/PTEN/AKT/FRAP pathway in human prostate cancer cells: implications for tumor angiogenesis and therapeutics," *Cancer Res.* **60**(6), 1541–1545 (2000).
38. H. P. Greenspan, "Models for growth of a solid tumor by diffusion," *Stud. Appl. Math.* **51**(4), 317–340 (1972).
39. S. Dormann and A. Deutsch, "Modeling of self-organized avascular tumor growth with a hybrid cellular automaton," *In Silico Biol.* **2**(3), 393–406 (2002).
40. L. Brannon-Peppas and J. O. Blanchette, "Nanoparticle and targeted systems for cancer therapy," *Adv. Drug Del. Rev.* **56**(11), 1649–1659 (2004).
41. F. Baowei, W. Hesheng, D. M. Joseph, K. F. Denise, L. O. Nancy, and L. D. Jeffrey, "High-field magnetic resonance imaging of the response of human prostate cancer to Pc 4-based photodynamic therapy in an animal model," *Lasers Surg. Med.* **39**(9), 723–730 (2007).
42. N. C. Silver and W. P. Dunlap, "Averaging correlation coefficients: Should Fisher's z transformation be used?," *J. Appl. Psychol.* **72**(1), 146–148 (1987).
43. B. Efron and R. Tibshirani, "Bootstrap methods for standard errors, confidence intervals, and other measures of statistical accuracy," *Stat. Sci.* **1**(1), 54–75 (1986).
44. E. A. Hendrickson, "The SCID mouse—relevance as an animal model system for studying human disease," *Am. J. Pathol.* **143**(6), 1511–1522 (1993).
45. J. Laufer, C. Elwell, D. Delpy, and P. C. Beard, "Pulsed near-infrared photoacoustic spectroscopy of blood," *Proc. SPIE* **5320**, 57 (2004).
46. X. D. Wang, X. Y. Xie, G. N. Ku, and L. H. V. Wang, "Noninvasive imaging of hemoglobin concentration and oxygenation in the rat brain using high-resolution photoacoustic tomography," *J. Biomed. Opt.* **11**(2), 024015 (2006).
47. H. F. Zhang, K. Maslov, M. Sivaramakrishnan, G. Stoica, and L. H. V. Wang, "Imaging of hemoglobin oxygen saturation variations in single vessels *in vivo* using photoacoustic microscopy," *Appl. Phys. Lett.* **90**(5), 053901 (2007).
48. J. Laufer, C. Elwell, D. Delpy, and P. Beard, "*In vitro* measurements of absolute blood oxygen saturation using pulsed near-infrared photoacoustic spectroscopy: accuracy and resolution," *Phys. Med. Biol.* **50**(18), 4409–4428 (2005).
49. L. V. Wang, X. Wang, G. Ku, X. Xie, and G. Stoica, "High-resolution spectroscopic photoacoustic tomography for noninvasive functional imaging of small-animal brains *in vivo*," *Biophotonics* 246–247 (2004).
50. M. L. Li, J. T. Oh, X. Y. Xie, G. Ku, W. Wang, C. Li, G. Lungu, G. Stoica, and L. V. Wang, "Simultaneous molecular and hypoxia imaging of brain tumors *in vivo* using spectroscopic photoacoustic tomography," *Proc. IEEE* **96**(3), 481–489 (2008).
51. S. Sethuraman, J. H. Amirian, S. H. Litovsky, R. W. Smalling, and S. Y. Emelianov, "Spectroscopic intravascular photoacoustic imaging to differentiate atherosclerotic plaques," *Opt. Express* **16**(5), 3362–3367 (2008).
52. S. Sethuraman, B. Wang, S. Litovsky, J. Amirian, R. Smalling, and S. Emelianov, "P0–2 spectroscopic intravascular photoacoustic imaging," *Proc. IEEE* 1188–1191 (2007).
53. Y. C. Shen, Z. H. Lu, S. Spiers, H. A. MacKenzie, H. S. Ashton, J. Hannigan, S. S. Freeborn, and J. Lindberg, "Measurement of the optical absorption coefficient of a liquid by use of a time-resolved photoacoustic technique," *Appl. Opt.* **39**(22), 4007–4012 (2000).
54. R. B. Barlow and M. L. Polanyi, "Absorption measurements for oxygenated and reduced hemoglobin in range 0.6–1.88 microns," *Clin. Chem.* **8**(1), 67–71 (1962).
55. R. O. Esenaliev, Y. Y. Petrov, O. Hartrumpf, D. J. Deyo, and D. S. Prough, "Continuous, noninvasive monitoring of total hemoglobin concentration by an optoacoustic technique," *Appl. Opt.* **43**(17), 3401–3407 (2004).
56. H. Key, E. R. Davies, P. C. Jackson, and P. N. T. Wells, "Optical attenuation characteristics of breast tissues at visible and near-infrared wavelength," *Phys. Med. Biol.* **36**(5), 579–590 (1991).
57. M. Hockel and P. Vaupel, "Tumor hypoxia: definitions and current clinical, biologic, and molecular aspects," *J. Natl. Cancer Inst.* **93**(4), 266–276 (2001).
58. F. Dehdashti, M. A. Mintun, J. S. Lewis, J. Bradley, R. Govindan, R. Laforest, M. J. Welch, and B. A. Siegel, "*In vivo* assessment of tumor hypoxia in lung cancer with 60Cu-ATSM," *Eur. J. Nucl. Med. Mol. Imaging* **30**(6), 844–850 (2003).
59. M. Hockel, K. Schlenger, B. Aral, M. Mitze, U. Schaffer, and P. Vaupel, "Association between tumor hypoxia and malignant progression in advanced cancer of the uterine cervix," *Cancer Res.* **56**(19), 4509–4515 (1996).
60. A. De La Zerda, C. Zavaleta, S. Keren, S. Vaithilingam, S. Bodapati, Z. Liu, J. Levi, B. R. Smith, T. J. Ma, O. Oralkan, Z. Cheng, X. Y. Chen, H. J. Dai, B. T. Khuri-Yakub, and S. S. Gambhir, "Carbon nanotubes as photoacoustic molecular imaging agents in living mice," *Nat. Nanotechnol.* **3**(9), 557–562 (2008).
61. S. Mallidi, J. Tam, T. Larson, A. Karpiouk, K. Sokolov, and S. Emelianov, "Selective detection of cancer using spectroscopic photoacoustic imaging and bioconjugated gold nanoparticles," *Proc. IEEE* 578–581 (2008).
62. P. Z. Vladimir, I. G. Ekaterina, V. S. Evgeny, K. Jin-Woo, G. K. Nikolai, and V. T. Valery, "Photoacoustic flow cytometry: principle and application for real-time detection of circulating single nanoparticles, pathogens, and contrast dyes *in vivo*," *J. Biomed. Opt.* **12**(5), 051503 (2007).
63. R. Olafsson, L. Montilla, P. Ingram, and S. R. Witte, "Tracking contrast agents using real-time 2D photoacoustic imaging system for cardiac applications," *Proc. SPIE* 7177, 71771R (2009).
64. L. Montilla, R. Olafsson, and R. S. Witte, "Real-time pulse echo and photoacoustic imaging using an ultrasound array and in-line reflective illumination," *Proc. SPIE* 7564, 75643C (2010).
65. L. Montilla, R. Olafsson, and R. S. Witte, "*In vivo* photoacoustic and pulse echo imaging of a pancreatic tumor using a hand held device," *Proc. IEEE UFFC* (in press) (2010).
66. S. A. Ermilov, T. Khamapirad, A. Conjusteau, M. H. Leonard, R. Lacewell, K. Mehta, T. Miller, and A. A. Oraevsky, "Laser optoacoustic imaging system for detection of breast cancer," *J. Biomed. Opt.* **14**(2), 024007 (2009).
67. S. Manohar, S. E. Vaartjes, J. C. G. van Hespen, J. M. Klaase, F. M. Van Den Engh, W. Steenbergen, and T. G. van Leeuwen, "Initial results of in vivo non-invasive cancer imaging in the human breast using near-infrared photoacoustics," *Opt. Express* **15**(19), 12277–12285 (2007).
68. Y. Jiechen, Y. Hao-Chung, L. Xiang, Z. Jun, Z. Qifa, H. Changhong, K. K. Shung, and C. Zhongping, "Integrated intravascular optical coherence tomography ultrasound imaging system," *J. Biomed. Opt.* **15**(1), 010512 (2010).